Contents lists available at ScienceDirect

Journal of Physics and Chemistry of Solids

journal homepage: www.elsevier.com/locate/jpcs

La$_{1-x}$Sr$_x$MO$_3$ (M = Co, Mn, Cr) interconnects in a 4-leg all-oxide thermoelectric generator at high temperatures

Reshma K. Madathil, Raphael Schuler, Truls Norby [*]

Department of Chemistry, Centre for Materials Science and Nanotechnology, University of Oslo, FERMiO, Gaustadalléen 21, NO-0349 Oslo, Norway

ABSTRACT

We herein report tests at high temperatures of a 4-leg oxide thermoelectric generator consisting of two pairs of p-type Ni$_{0.98}$Li$_{0.02}$O (Li–NiO) and n-type Zn$_{0.98}$Al$_{0.02}$O (Al–ZnO), assembled with various conducting perovskite oxides as interconnects. Using a custom-built testing system, we evaluated performance and stability at a hot side (furnace) temperature of up to 1000 °C under temperature differences up to ΔT = 600 °C in air. With a La$_{0.6}$Sr$_{0.4}$CoO$_3$ (LSC) interconnect, a maximum power output of 18 mW was achieved with T_H = 940 and T_C = 340 °C (ΔT = 600 °C). Power maxima with La$_{0.8}$Sr$_{0.2}$MnO$_3$ (LSM) and La$_{0.8}$Sr$_{0.2}$CrO$_3$ (LSCr) as interconnects were lower, 6 mW and 2 mW, respectively, under similar conditions, attributed to their lower thermal and electrical conductivities. This demonstrates the requirements and potential of oxide interconnects for stable use of all-oxide thermoelectric generators at high temperatures in ambient air.

1. Introduction

Thermoelectric generators (TEGs) are highly reliable solid-state devices that directly convert heat into electrical energy without any moving parts. Most commercially available TEGs are chalcogenide based materials such as Bi$_2$Te$_3$, Pb–Te, etc. [1] Toxicity, poor thermal and chemical stability, and high processing costs limit their extensive applications irrespective of their excellent performance [2]. Metal oxides are alternative candidates for high-temperature TEGs because of their low cost and toxicity and good thermochemical stability including oxidation resistance. The figures of merit (zT) for oxide thermoelectric (TE) materials are generally inferior to non-oxides, but various layered cobalt-containing p-type oxides exhibit high power factors [3,4]. Among the fewer n-type oxides that operate stably under oxidising conditions, CaMnO$_3$ based perovskites and doped ZnO are attractive [5,6]. According to some studies, the oxide-based TEG devices often show lower performance than expected from their parent material properties [7,8]. This is due to the high contact resistance at the oxide/metal junctions after high temperature usages. These metals oxidise at high temperatures and limit the final device performance. Cracking and exfoliation of the contact deteriorate the interface and progressively decrease the device activity [9–11]. Low contact resistance between thermoelement materials and interconnect are essential to achieve the best device performance. The conventional metal interconnects like Pt, Au and Ag

cannot form an ohmic contact with both p and n oxide at a time and thus leads to a high contact resistance at the interface. It is not easy to choose a best interconnect material which compatible with both oxide TE for high temperature applications. So far, the best interconnect material used for oxide devices is metal-oxide composite of corresponding oxide materials with noble metals [12]. And many oxide devices prefer this metal-oxide composite interconnects concept for best device performance [8,13].

Perovskite-based oxides with high electronic conductivity are widely employed as cathodes, interconnects and protective coating for metal interconnects in solid oxide fuel cells (SOFC) [14].

Here, we explore such oxides as interconnects for oxide TEGs at high temperature in air, namely Sr-doped lanthanum cobaltite (La$_{0.6}$Sr$_{0.4}$CoO$_3$, LSC), manganite (La$_{0.8}$Sr$_{0.2}$MnO$_3$, LSM), and chromite (La$_{0.8}$Sr$_{0.2}$CrO$_3$, LSCr). They are all p-type conductors with conductivities at 100–1000 °C of 1000–1500 S/cm for LSC [15,16], 10–200 S/cm for LSM [17], and 3–14 S/cm for LSCr [18]. LSC and LSM are used in SOFC cathodes [19–22], while LSCr is used as interconnect in SOFCs and heating elements in high temperature furnaces [23–25].

We explore the device performance of a 4-leg thermoelectric module of p-type NiO and n-type ZnO using a newly developed test unit [26]. NiO is a p-type semiconductor with a wide bandgap above 3.6 eV and Li-doping greatly enhances its conductivity for use in high temperature thermoelectric applications [27,28]. ZnO is an intrinsic n-type
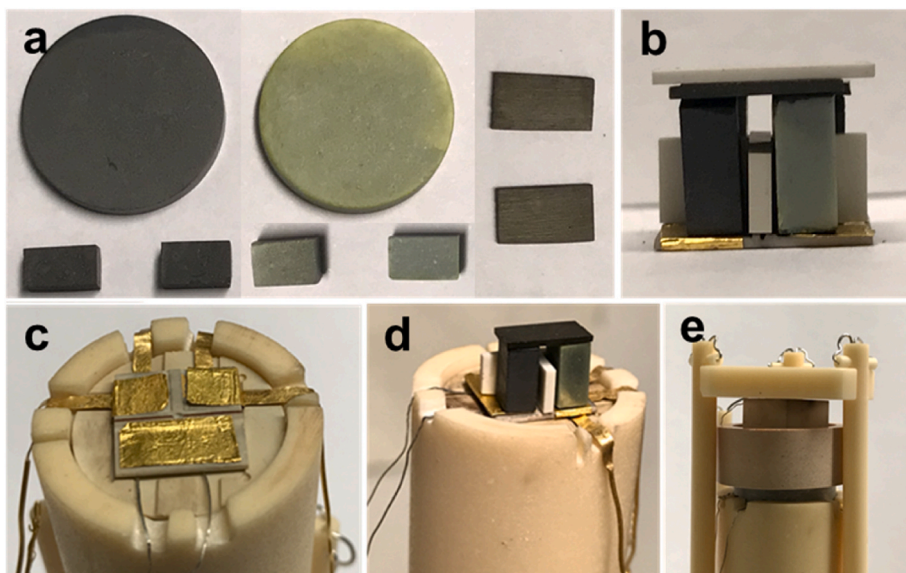

Fig. 1. Photographs of the different steps in the manufacturing of legs and other parts and fabrication of the oxide thermoelectric module. (a) NiO, ZnO TE elements and LSC interconnects, (b) leg assembly in π-shape, (c) the bottom part of the module-testing unit with Au contacts and a type S thermocouple, (d) module assembled on the testing set up, and (e) final view of the overall testing unit including module housing, top type S thermocouple, and spring load. The outer ceramic tube in c)-e) encloses a stainless steel support-tube (not visible) that is flushed with water and cools the bottom part of the module. The entire setup is enclosed in an outer quartz tube and inserted in a vertical tubular furnace.
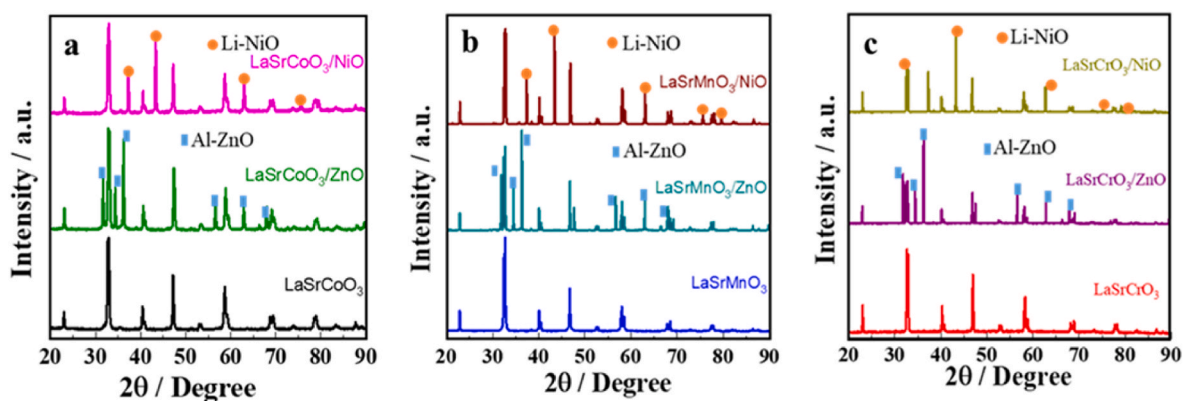
Fig. 2. XRD patterns of individual oxides and their powder mixtures with NiO and ZnO: (a) LSC, (b) LSM, and (c) LSCr.
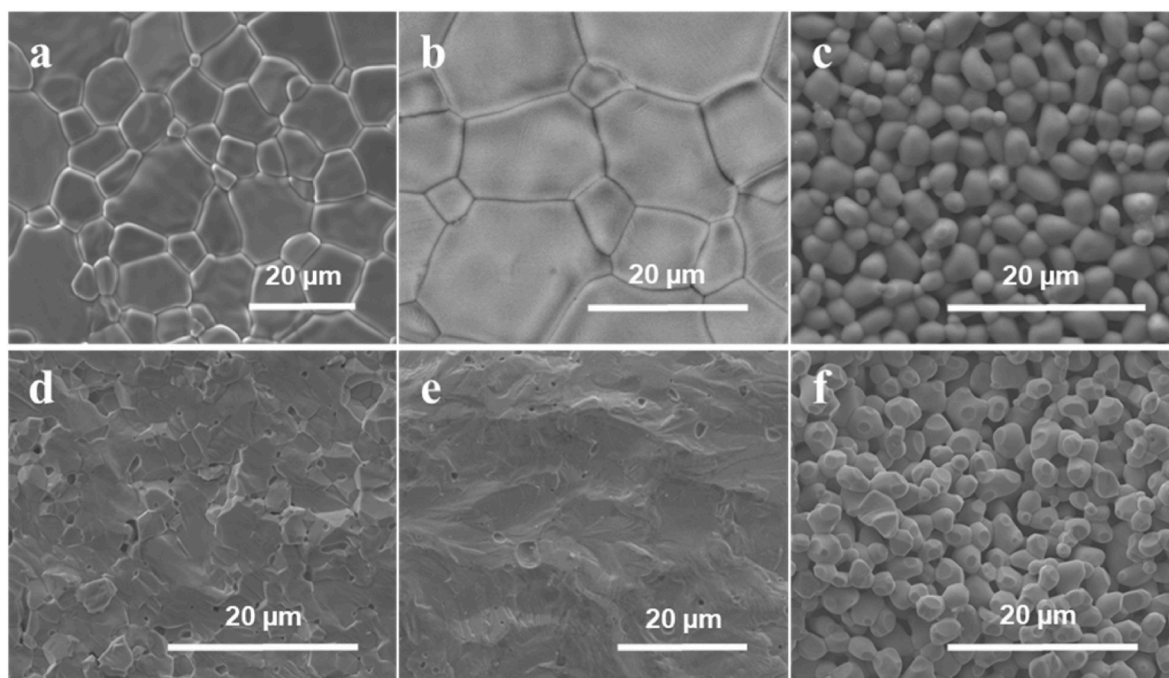
Fig. 3. SEM top view (a,b,c) and cross-sectional view (d,e,f) of, respectively, LSC, LSM. and LSCr.
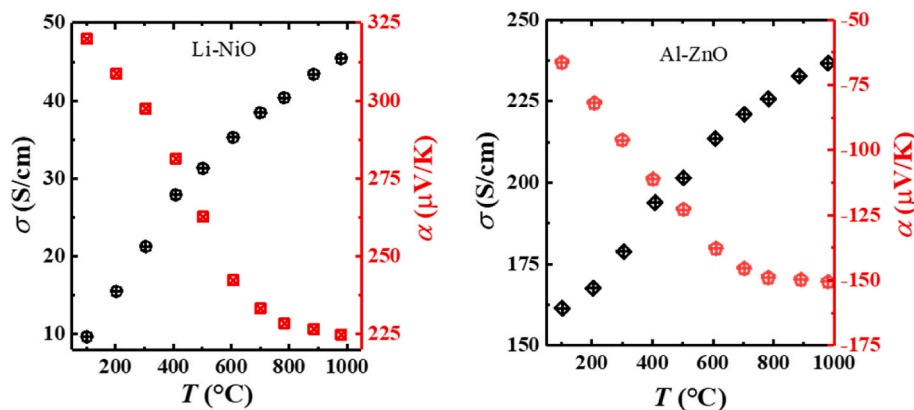
Fig. 4. Thermoelectric properties of the p-type $Ni_{0.98}Li_{0.02}O$ (left) and n-type $Zn_{0.98}Al_{0.02}O$ (right).

semiconductor with a bandgap of around 3.3 eV, and here donor doping with Al is commonly used to enhance the electrical conductivity [29, 30]. This paper describes the performance of all-oxide 4-leg thermo-electric TEGs fabricated with two pairs of Li–NiO and Al–ZnO and LSC, LSM, or LSCr integrated as interconnects.

2. Experimental procedures

ZnO (Sigma Aldrich, 99.99%) and $Al(NO_3)_3 \cdot 9H_2O$ were used as precursors to prepare $Zn_{0.98}Al_{0.02}O$, while NiO (Sigma Aldrich, 99.97%) and $LiNO_3$ (Merck, 99.9%) were starting materials for $Ni_{0.98}Li_{0.02}O$. The precursors were ball milled in isopropanol with jar and balls of stabilised zirconia for 24 h followed by calcination at 800 °C for 5 h. Disks were uniaxially cold-pressed and then sintered at 1400 °C for 10 h. The perovskite materials $La_{0.6}Sr_{0.4}CoO_3$, $La_{0.8}Sr_{0.2}MnO_3$, and $La_{0.8}Sr_{0.2}CrO_3$ were synthesised by a modified solid-state route [31–36]. Appropriate amounts of La_2O_3, Co_3O_4, $MnCO_3$, Cr_2O_3 and $SrCO_3$ powders were mixed in isopropanol and ball milled for 20 h for LSC and LSM and 24 h for LSCr. The products were dried and calcined at temperatures between 800 and 1100 °C for 5–10 h. Then the powders were uniaxially pressed into green compacts and sintered for 10 h at 1300, 1400, and 1600 °C for LSC, LSM, and LSCr, respectively. They were finally cut and ground into strips 0.5 mm thick for use as interconnects.

A π-shaped thermoelectric device was fabricated using two pairs of Li–NiO and Al–ZnO. The leg manufacture and module assembly steps are illustrated in Fig. 1, further details are described elsewhere [26]. The dense pellets of NiO and ZnO were cut and ground into rectangular legs $4.5 \times 4.5 \times 6$ mm^3 using an Allied Hightech TechCut 4x™. The two p-n couples were linked together by the strips of conducting oxide in-terconnects. For additional electrical contact and compatibility with the set-up, the bottom end of each TE leg was coated with perovskite interconnect and then placed on top of a 0.05 mm thick gold (Au) foil contact (Fig. 1c). Hence, at the cold side, the top face of the interconnect is in contact with the TE leg, and the bottom face is in direct contact with the Au foil. There is no additional interlayer between the TE leg and interconnect on the hot side. A spring-load system holds the 4-leg module in a ProboStat™ measurement cell (NorECs, Norway). As shown in Fig. 1b, the oxide module was intact after tests, demonstrating thermochemical stability and compatibility of the materials involved for application at high temperatures up to 1000 °C in air.

3. Characterization

A Bruker D8 X-ray diffractometer with Cu-Kα radiation was used to verify the crystal structure and phase purity of the perovskite powders and a mixture of these oxides with the TE leg materials (see Fig. 2). The XRD analyses show that all three (LSC, LSM, LSCr) perovskite samples are phase pure. To check the chemical compatibility of these in-terconnects towards the thermoelectric leg materials, they were mixed and heated at 1000 °C for 50 h. The XRD results showed only the initial two phases, with no deviation in the XRD peak position and no addi-tional peaks corresponding to any reaction product phases. These results confirm the stability of the materials in contact with each other, although some interdiffusion of cations cannot be excluded.

The microstructural characterization of the three interconnect ma-terials was done with FEI Quanta 200 F FEG-ESEM, see Fig. 3. Scanning Electron Microsopy (SEM) was performed on the surface and fracture of the pellets in backscatter electron mode. Fig. 3 (a) and (b) show the dense surfaces of LSC (relative density (RD) ~ 90%) and LSM (RD ~94%), respectively, evidencing considerable grain growth, while (c) shows LSCr with high porosity (RD ~70%) and little grain growth. This was further evidenced in the cross-sectional views of the pellets (d-f).

4. Results and discussion

The temperature dependencies of the thermoelectric properties (electrical conductivity and Seebeck coefficient) of the p-type Li–NiO
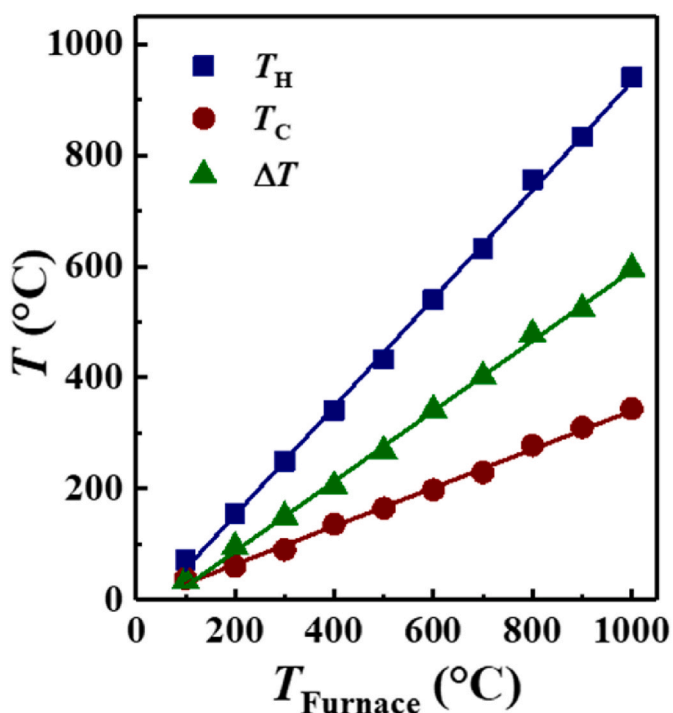

Fig. 5. Temperatures measured by the hot and cold side thermocouples and the resulting difference over the module as a function of furnace temperature.
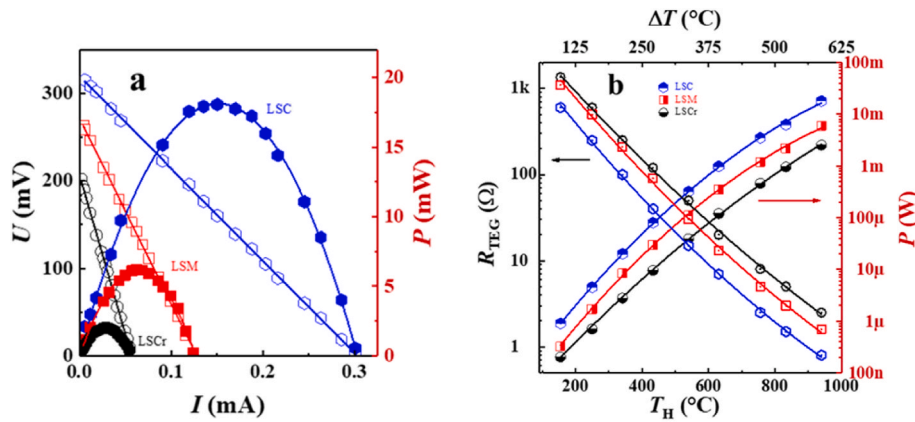
Fig. 6. (a) The module characteristics at furnace temnperature of 1000 °C for a 4-leg module with three different interconnects. (b) The measured temperature dependencies of module resistance and calculated maximum power output of the module.

and n-type Al–ZnO were measured in a customized setup [37] and are displayed in Fig. 4, generally consistent with previously reported studies [38,39]. The thermal conductivities of these materials are reported in the ranges of 20–5 W/mK for Li–NiO and 35-8 W/mK for Al–ZnO for the temperature range 100–700 °C [26,38,40]. The interdiffusion and electrical properties of direct p-n junctions between these materials at high temperatures have been reported elsewhere [41,42], but in this study they are not in direct contact as they are separated by interconnect oxides.

The hot side and cold side temperature (T_H and T_C) in the 4-leg module setup measured by individual thermocouples and the resulting temperature difference (ΔT) are given as a function of the furnace temperature in Fig. 5.

The theoretical open circuit voltage ($OCV_{Theoretical}$) can be calculated from

$$OCV_{Theoretical} = N(\alpha_p - \alpha_n)\Delta T \tag{1}$$

where N is the number of p-n pairs, α is the individual effective Seebeck coefficient averaged over the temperature difference ΔT. Hence the current can be expressed as

$$I = \frac{N(\alpha_p - \alpha_n)\Delta T}{R_{TEG} + R_L} \tag{2}$$

Here, R_L is the external load resistance, while R_{TEG} is the sum of resistances of individual thermoelectric materials R_{TE}, the interconnect resistance R_{IC} and the interface contact resistance R_C:

$$R_{TEG} = R_{TE} + R_{IC} + R_C \tag{3}$$

The power generation can be calculated using the following equation

$$P = I^2 R_L \tag{4}$$

The maximum power output occurs when $R_L = R_{TEG}$ and the P_{max} is related to the measured open-circuit voltage (OCV) and resistance as per the following equation,

$$P_{max} = \frac{OCV^2}{4R_{TEG}} \tag{5}$$

The results of testing the thermoelectric performance of the 4-leg module with three different interconnect are summarized in Fig. 6. The I–P and I–U curve for the present 4-leg oxide module at a specific furnace temperature of 1000 °C ($T_H = 940$ °C and $\Delta T = 600$ °C) is given in Fig. 6a.

The electrical power generation characteristics of the oxide thermoelectric module were measured from 100 °C to 1000 °C with a minimum equilibration time of 1 h. In order to obtain the I–U curve, the voltage of the module was measured via separate voltage contacts, and

the corresponding current was controlled using a resistance switch box. We extracted the measured OCV values from the I–U measurements and calculated the power output using Eq. (4). The temperature dependencies of power output and resistance of the module with three different interconnect materials are compared in Fig. 6b. The electrical power output is at maximum (P_{max}) when the load resistance R_L is equal to R_{TEG}, and is from Eq. (5) a function of the OCV and R_{TEG}.

$OCV_{Theoretical}$ calculated from Eq. (1) is plotted along with the measured OCV for the TEGs with different interconnects in Fig. 7. The measured OCV with LSC was 315 mV at a furnace temperature of 1000 °C as compared to the $OCV_{Theoretical}$ ~446 mV and remained around 70% at all temperatures. In comparison, the OCV with LSM and LSCr interconnects were around 60% and 45%, respectively, of theoretical. This may reflect the difference in thermal coupling between the imposed temperature gradient and the hot and cold ends of the TE leg materials. The thermal conductivity κ of LSC is 2.5–6 W/mK for LSC at
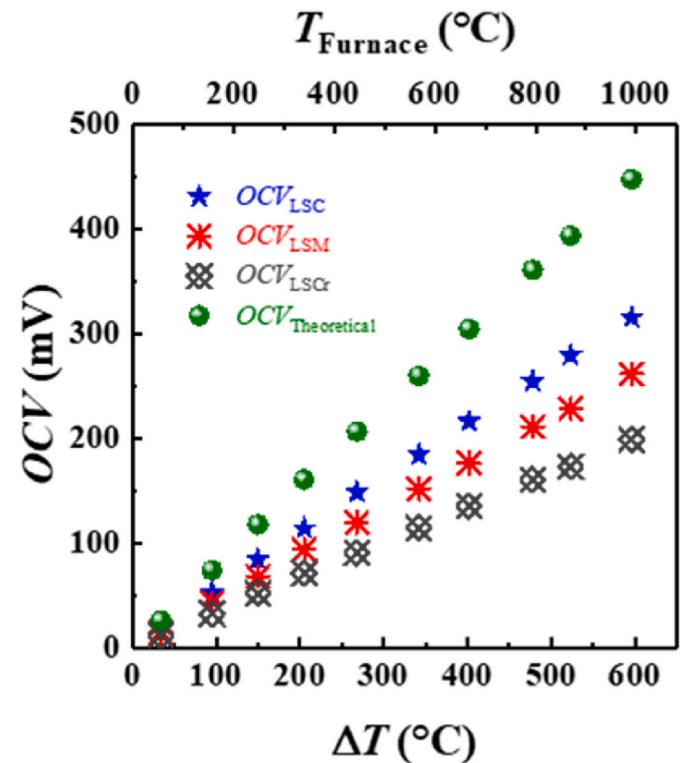

Fig. 7. Theoretical and measured open-circuit voltages (OCV) for the 4-leg module as a function of measured temperature difference.
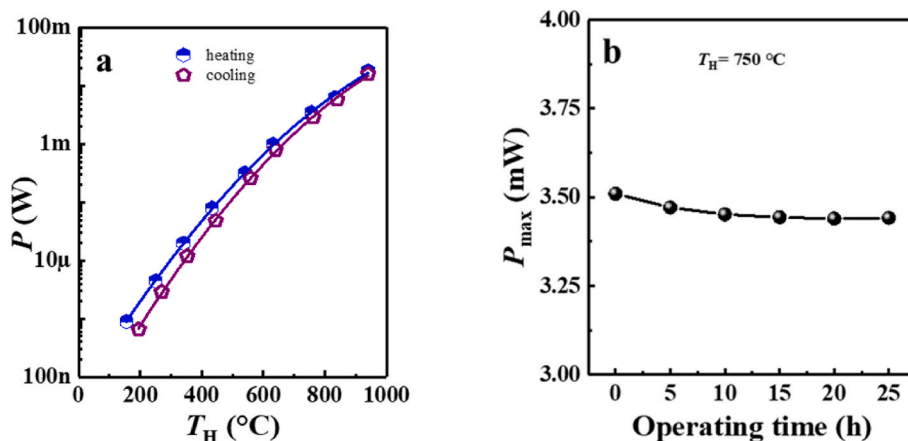
Fig. 8. (a) Hot side temperature dependence of maximum output power evaluated for the heating-cooling cycle in a module with LSC interconnect and (b) Change of P_{max} of the device with LSC interconnect isothermally operated in the air at $T_H = 750$ °C.

Table 1
Comparison of specification, running condition, and performance of various oxide thermoelectric modules.

Materials	No: of p-n couples	Joining technique (interconnect)	T_H (K)	ΔT (K)	P_{max} (mW)	Ref
p-$Li_{0.025}Ni_{0.975}O$ n-$Ba_{0.4}Sr_{0.6}PbO_3$	4	Sintering	1164	539	34.4	[51]
p-$NaCo_{1.7}Cu_{0.3}O_4$ n-$Ba_{0.4}Sr_{0.6}PbO_3$	1	Au-Foil	1045	506	12	[52]
p-$Na_{0.7}CoO_2$ n-$Ca_{0.92}La_{0.08}MnO_3$	2	Ag–Pd electrodes	618	554	7.6	[53]
p-$Ca_{2.7}Bi_{0.3}Co_4O_9$ n-$La_{0.9}Bi_{0.1}NiO_3$	1	Ag paste with oxide powder	1073	500	94	[12]
p-$NaCo_2O_4$ n-$Zn_{0.98}Al_{0.02}O$	12	Ag plate Diffusion welding	934	455	52.5	[54]
p-$GdCo_{0.95}Ni_{0.05}O_3$ n-$CaMn_{0.98}Nb_{0.02}O_3$	2	Ag/CuO	800	500	47	[55]
p-$Ca_3Co_4O_9$ n-$(ZnO)_7In_2O_3$	44	Ag-paste	1100	673	423	[56]
p-$Ca_3Co_{4-x}O_{9+\delta}$ n-$CaMnO_{3-\delta}/CaMn_2O_4$	1	Spark plasma co-sintering	1173	923	7.2	[57]
p-$Ni_{0.98}Li_{0.02}O$ n-$Zn_{0.98}Al_{0.02}O.$	2	Au Foil	1103	813	7.3	[26]
p-$Ni_{0.98}Li_{0.02}O$ n-$Zn_{0.98}Al_{0.02}O.$	2	Conducting oxide $La_{0.6}Sr_{0.4}CoO_3$	1213	873	18	This work

300–1000 K [43], while κ for LSM is in the range 2.2–4 W/mK [44,45], and that for LSCr is 1–2 W/mK [46].

The P_{max} values decrease with decreasing temperatures, as expected mainly from the temperature dependencies of the electrical conductivities of the leg materials. A maximum power output (P_{max}) of 18 mW was derived with LSC as interconnect material at a furnace temperature of 1000 °C, while it decreased to 6 mW and 2 mW with LSM and LSCr, respectively, as shown in Fig. 6b. This can be attributed to the difference in conductivities of the interconnects and high contact resistance at the interface. We have recently reported the low interface contact resistance for a NiO–ZnO junction with LSC as interconnect [47].

The maximum power output (P_{max}) as a function of hot side temperature (both heating and cooling cycle) of the four-leg test module with LSC as interconnect are depicted in Fig. 8a. The power output was slightly decreased during cooling compared to heating, especially at the lower temperature region. It might be due to the deterioration of the ZnO conductivity by segregation of a low-conducting spinel $ZnAl_2O_4$ phase during heating [48–50].

The durability of the device was investigated by continuous operation under thermal conditions $T_H = 750$ °C and $\Delta T = 470$ °C in air, and the P_{max} value is plotted against the operating time (given in Fig. 8b). The P_{max} value was almost constant during continuous operation for 25 h, indicating the module's high reliability and the slight decrease in output power was expected due to the deterioration of Al–ZnO.

The specification, condition and performance of our module was compared with that of other selected oxide–based modules developed thus far and summarized in Table 1. The present oxide thermoelectric module has a similar configuration listed in reference [26] but differs in the interconnect used. Our module showed improved performance compared to the reference in the same testing condition but still has a significant loss in *OCV* compared to the theoretical voltage. The findings of this study point out the importance of the use of non-metallic interconnects for oxide TEGs. Further improvement of the power generation performance of the module and more research to lower the voltage losses are still needed.

5. Conclusion

A practical thermoelectric module was fabricated based on two pairs of Li–NiO and Al–ZnO. We have successfully tested a prototype oxide thermoelectric module with different conducting oxides as interconnects - a new concept for oxide thermoelectrics. The absence of additional peaks for new phases in the XRD analysis confirms the chemical stability between the legs and interconnect materials under operating conditions. The overall performance of the device built with $4.5 \times 4.5 \times 6$ mm³ legs and different interconnect materials was determined from 100 to 1000 °C furnace temperature. With LSC, LSM and LSCr as interconnect materials, the two pair (4-leg) module displayed *OCVs* of 236, 184, and

137 mV, respectively, and maximum power outputs of 18, 6, and 2 mW at a furnace temperature of 1000 °C, $T_H = 940$ °C, and $\Delta T \approx 600$ °C in air. The difference in *OCV* and power is tentatively attributed to the difference in thermal and electrical conductivities of the three interconnects.

Author credit statement

Reshma K. Madathil: Investigation; Validation; Visualization; Writing - original draft; Writing - review & editing. **Raphael Schuler:** Methodology; Validation; Writing - review & editing. **Truls Norby:** Conceptualization; Funding acquisition; Methodology; Project administration; Resources; Supervision; Writing - review & editing.

Declaration of competing interest

The authors declare that they have no known competing financial interests or personal relationships that could have appeared to influence the work reported in this paper.

References

[1] S. LeBlanc, Thermoelectric generators: linking material properties and systems engineering for waste heat recovery applications, Sustain. Mater. Technol. 1–2 (2014) 26–35.
[2] J.W. Fergus, Oxide materials for high temperature thermoelectric energy conversion, J. Eur. Ceram. Soc. 32 (3) (2012) 525–540.
[3] Y. Feng, et al., Metal oxides for thermoelectric power generation and beyond, Adv. Comp. Hybrid Mater. 1 (1) (2018) 114–126.
[4] Y.-H. Lin, J. Lan, C. Nan, Oxide Thermoelectric Materials: from Basic Principles to Applications, John Wiley & Sons, 2019, pp. 133–151.
[5] N. Pryds, R. Bjørk, Oxide thermoelectrics: from materials to module, in: O. Guillon (Ed.), Advanced Ceramics for Energy Conversion and Storage, Elsevier, 2020, pp. 131–156.
[6] J. He, Y. Liu, R. Funahashi, Oxide thermoelectrics: the challenges, progress, and outlook, J. Mater. Res. 26 (15) (2011) 1762–1772.
[7] I. Matsubara, et al., Fabrication of an all-oxide thermoelectric power generator, Appl. Phys. Lett. 78 (23) (2001) 3627–3629.
[8] K. Arai, et al., Improvement of electrical contact between TE material and Ni electrode interfaces by application of a buffer layer, J. Electron. Mater. 41 (6) (2012) 1771–1777.
[9] M. Zebarjadi, et al., Perspectives on thermoelectrics: from fundamentals to device applications, Energy Environ. Sci. 5 (1) (2012) 5147–5162.
[10] W. Wu, et al., Interfacial advances yielding high efficiencies for thermoelectric devices, J. Mater. Chem. 9 (6) (2021) 3209–3230.
[11] R. He, G. Schierning, K. Nielsch, Thermoelectric devices: a review of devices, architectures, and contact optimization, Adv. Mater. Technol. 3 (4) (2018), 1700256.
[12] R. Funahashi, et al., Ca$_{2.7}$Bi$_{0.3}$Co$_4$O$_9$/La$_{0.9}$Bi$_{0.1}$NiO$_3$ thermoelectric deviceswith high output power density, Appl. Phys. Lett. 85 (5) (2004) 1036–1038.
[13] R. Funahashi, et al., A portable thermoelectric-power-generating module composed of oxide devices, J. Appl. Phys. 99 (6) (2006), 066117.
[14] A. Brouzgou, A. Demin, Interconnects for Solid Oxide Fuel Cells, 2017, pp. 119–153.
[15] J. Mizusaki, et al., *Electronic conductivity, Seebeck coefficient, and defect Structure of La$_{1-x}$Sr$_x$FeO$_3$ (x=0.l, 0.25)*, J. Am. Ceram. Soc. 66 (4) (1983) 247–252.
[16] Z. Zhu, et al., Improving electronic conductivity and oxygen reduction activity in Sr-doped lanthanum cobaltite thin films: cobalt valence state and electronic band structure effects, ACS Appl. Energy Mater. 1 (10) (2018) 5308–5317.
[17] A. Berenov, H. Wood, A. Atkinson, Evaluation of La$_{0.8}$Sr$_{0.2}$Cu$_{1-x}$Mn$_x$O$_{3-d}$ double Perovskite for Use in SOFCs, ECS Transact. 7 (1) (2019) 1173–1181.
[18] Y.-J. Yang, et al., Characteristics of lanthanum strontium chromite prepared by Glycine nitrate process, Solid State Ionics 135 (2000) 475–479.
[19] M.Y. Oh, et al., The bifunctional electrocatalytic activity of perovskite La$_{0.6}$Sr$_{0.4}$CoO$_{3-\delta}$ for oxygen reduction and evolution reactions, RSC Adv. 5 (25) (2015) 19190–19198.
[20] N. Alhokbany, et al., *Investigation of structural and electrical properties of synthesized Sr-doped lanthanum cobaltite (La$_{1-x}$Sr$_x$CoO$_3$) perovskite oxide*, J. King Saud Univ. Sci. 33 (4) (2021), 101419.
[21] S. Jiang, Development of lanthanum strontium manganite perovskite cathode materials of solid oxide fuel cells: a review, J. Mater. Sci. 43 (2008) 6799–6833.
[22] H. Arandiyan, et al., *Three-dimensionally ordered macroporous La$_{0.6}$Sr$_{0.4}$MnO$_3$ with high surface areas: Active catalysts for the combustion of methane*, J. Catal. 307 (2013) 327–339.
[23] P. Sujatha Devi, M. Subba Rao, *Preparation, structure, and properties of strontium-doped lanthanum chromites: La$_{1-x}$Sr$_x$CrO$_3$*, J. Solid State Chem. 98 (2) (1992) 237–244.
[24] J.W. Fergus, Lanthanum chromite-based materials for solid oxide fuel cell interconnects, Solid State Ionics 171 (1) (2004) 1–15.
[25] H. Qi, et al., Preparation, characterization and electrical properties of Ca and Sr doped LaCrO$_3$, Inorg. Chem. Commun. 66 (2016) 33–35.
[26] R. Schuler, R.K. Madathil, T. Norby, Versatile four-leg thermoelectric module test setup adapted to a commercial sample holder system for high temperatures and controlled atmospheres, Rev. Sci. Instrum. 92 (4) (2021), 043902.
[27] A. Bosman, C. Crevecoeur, Mechanism of the electrical conduction in Li-doped NiO, Phys. Rev. 144 (2) (1966) 763.
[28] I. Hotový, et al., The influence of process parameters and annealing temperature on the physical properties of sputtered NiO thin films, Vacuum 69 (1) (2002) 237–242.
[29] K.C. Park, D.Y. Ma, K.H. Kim, The physical properties of Al-doped zinc oxide films prepared by RF magnetron sputtering, Thin Solid Films 305 (1) (1997) 201–209.
[30] Z.L. Wang, Zinc oxide nanostructures: growth, properties and applications, J. Phys. Condens. Matter 16 (25) (2004) R829–R858.
[31] F. Boroomand, et al., *Correlation between defect chemistry and expansion during reduction of doped LaCrO$_3$ interconnects for SOFCs*, Solid State Ionics 129 (1) (2000) 251–258.
[32] Q. Zhang, T. Nakagawa, F. Saito, *Mechanochemical synthesis of La$_{0.7}$Sr$_{0.3}$MnO$_3$ by grinding constituent oxides*, J. Alloys Compd. 308 (1) (2000) 121–125.
[33] G. Velciu, et al., *LaCoO$_3$ synthesis by intensive mechanical activation*, Ceram. Int. 41 (5) (2015) 6876–6881. Part B).
[34] P.H. Duvigneaud, P. Pilate, F. Cambier, *Factors affecting the sintering and the electrical properties of Sr-doped LaCrO$_3$*, J. Eur. Ceram. Soc. 14 (4) (1994) 359–367.
[35] H. Ahmed, et al., A comparative study of Sr-doped LaMnO$_3$ synthesised via solid-state reaction and sol–gel methods, Phil. Mag. Lett. 98 (9) (2018) 365–374.
[36] H. Kozuka, et al., *Origin of high electrical conductivity in alkaline-earth doped LaCoO$_3$*, J. Mater. Chem. 22 (22) (2012) 11003–11005.
[37] M. Schrade, et al., Versatile apparatus for thermoelectric characterization of oxides at high temperatures, Rev. Sci. Instrum. 85 (10) (2014), 103906.
[38] W. Shin, N. Murayama, Li-doped nickel oxide as a thermoelectric material, Jpn. J. Appl. Phys. 38 (2) (1999) L1336–L1338. No. 11B.
[39] C. Qi, et al., *Utilizing of high-pressure high-temperature synthesis to enhance the thermoelectric properties of Zn$_{0.98}$Al$_{0.02}$O with excellent electrical properties*, Chin. Phys. B 30 (2021), 016202.
[40] F. Giovannelli, et al., Thermal conductivity and stability of Al-doped ZnO nanostructured ceramics, J. Eur. Ceram. Soc. 38 (15) (2018) 5015–5020.
[41] T.D. Desissa, et al., Inter-diffusion across a direct p-n heterojunction of Li-doped NiO and Al-doped ZnO, Solid State Ionics 320 (2018) 215–220.
[42] T.D. Desissa, M. Schrade, T. Norby, Electrical properties of a p–n heterojunction of Li-doped NiO and Al-doped ZnO for thermoelectrics, J. Electron. Mater. 47 (9) (2018) 5296–5301.
[43] M.A. Bousnina, et al., Synthesis, sintering, and thermoelectric properties of the solid solution La1–xSrxCoO3±δ (0 ≤ x ≤ 1), J. Adv. Ceram. 7 (2) (2018) 160–168.
[44] H. Fujishiro, S. Kanoh, M. Ikebe, Heat transport Enhancement in ferromagnetic metallic Phase of La$_{1-x}$Ba$_x$MnO$_3$, J. Phys. Soc. Jpn. 71 (Suppl) (2002) 142–144.
[45] J.L. Cohn, et al., Local lattice distortions and thermal transport in perovskite manganites, Phys. Rev. B 56 (14) (1997) R8495–R8498.
[46] W.J. Weber, C.W. Griffin, J.L. Bates, *Effects of cation Substitution on Electrical and thermal transport Properties of YCrO$_3$ and LaCrO$_3$*, J. Am. Ceram. Soc. 70 (4) (1987) 265–270.
[47] R.K. Madathil, T. Norby, Lanthanum strontium cobaltite as interconnect in oxide thermoelectric generators, Solid State Sci. 124 (2022), 106801.
[48] J. Mayandi, et al., Al-doped ZnO prepared by co-precipitation method and its thermoelectric characteristics, Mater. Lett. 288 (2021), 129352.
[49] D. Bérardan, C. Byl, N. Dragoe, Influence of the preparation conditions on the thermoelectric properties of Al-doped ZnO, J. Am. Ceram. Soc. 93 (8) (2010) 2352–2358.
[50] S. Yang, et al., Microstructure and electrical properties of AZO/graphene nanosheets fabricated by spark plasma sintering, Materials 9 (8) (2016) 638.
[51] W. Shin, et al., Fabrication of oxide thermoelectric generator element, Jpn. J. Appl. Phys. 39 (3A) (2000) 1254–1255.
[52] W. Shin, et al., *Thermoelectric Device of Na(Co,Cu)$_2$O$_4$ and (Ba,Sr)PbO$_3$*, J. Ceram. Soc. Jpn. 110 (1284) (2002) 727–730.
[53] Y. Ono, et al., Fabrication and performance of an oxide thermoelectric power generator, in: Twenty-First International Conference on Thermoelectrics, 2002 2, Proceedings ICT, 2002, pp. 454–457.
[54] S. Takeshi, et al., Power generation characteristics of oxide thermoelectric modules incorporating nanostructured ZnO sintered materials, in: 2007 26th International Conference on Thermoelectrics, 2007, pp. 38–41.
[55] P. Tomeš, et al., Synthesis and characterization of new ceramic thermoelectrics implemented in a thermoelectric oxide module, J. Electron. Mater. 39 (9) (2010) 1696–1703.
[56] S.-M. Choi, et al., *Oxide-based thermoelectric power generation module using p-type Ca$_3$Co$_4$O$_9$ and n-type (ZnO)7In$_2$O$_3$ legs*, Energy Convers. Manag. 52 (1) (2011) 335–339.
[57] N. Kanas, et al., Time-enhanced performance of oxide thermoelectric modules based on a hybrid p–n junction, ACS Omega 6 (1) (2021) 197–205.